Al-Qadisiyah JournalFor Engineering Sciences 18 (2025) 336–344

Contents lists available at: http://qu.edu.iq

Al-Qadisiyah Journal for Engineering Sciences

Journal homepage: https://qjes.qu.edu.iq

Research Paper

Printability and strength of 3D-printed concrete: Role of mix design and printing parameters

Marwah M. Thajeel [1]✉, ***Ameen H. Chalawi*** [2], ***and György L. Balázs*** [1]

[1]*Department of Construction Materials and Technologies, Faculty of Civil Engineering, Budapest University of Technology and Economics, Budapest, Hungary.*
[2]*Department of Engineering Geology and Geotechnics, Faculty of Civil Engineering, Budapest University of Technology and Economics, Budapest, Hungary.*

ARTICLE INFO

Article history:
Received 14 December 2024
Received in revised form 08 February 2025
Accepted 01 September 2025

keyword:
Anisotropy
Compressive strength
Printing paths
Rheological properties
Supplementary cementitious materials
3D printed concrete

ABSTRACT

This study investigates the properties of 3D printed concrete mixtures, focusing on rheological characteristics, compressive strength, anisotropy, and printing path effects. Two mixtures were compared: M-1 (90% cement, 10% metakaolin) and M-2 (85% cement, 10% metakaolin, 5% silica fume). M-2 demonstrated superior performance in flowability, shape retention, and buildability, allowing for 164% more printed layers than M-1. Compressive strength tests revealed that 3D-printed specimens consistently exhibited lower strength compared to cast specimens due to layering effects and anisotropy. M-2 showed higher compressive strength in both cast and printed cubes. Significant anisotropy was observed in mechanical properties, with compressive strength highest in the X direction and lowest in the Y direction. Flexural strength and elastic modulus also varied depending on the loading direction. Among printing patterns, the zigzag pattern with 90-degree rotation between layers (P1) exhibited the highest compressive strength, while circular patterns (P2) showed the lowest. These findings emphasize the importance of optimizing mix design, printing parameters, and loading direction considerations for 3D-printed concrete structures.

1. Introduction

Concrete is one of the most widely used man-made composite materials globally, with its popularity steadily increasing since its inception. It is a key material in various civil engineering applications, including buildings, roads, dams, retaining walls and bridges. Currently, the demand for concrete remains high and is expected to grow in the future. However, traditional concrete cannot be classified as an environmentally sustainable material due to concerns related to the depletion of natural resources, high energy consumption, and challenges associated with construction waste management [1]. Additive Manufacturing (AM), commonly referred to as 3D-printing, has emerged as a transformative technology capable of fabricating three-dimensional objects layer by layer. Over recent years, AM has evolved rapidly within the construction industry [2, 3]. This digital technology enables enhanced flexibility in concrete manufacturing while optimizing material utilization. With the rising global demand for housing, there is an urgent need to adopt advanced construction methods. Among these, 3D-printed prefabricated building blocks offer a promising solution, paving the way for more efficient housing production [4] Formwork costs account for nearly 80% of a project's total expenses [2]. Moreover, it generates significant construction waste, restricts geometric freedom, and limits architects' creativity. Complex shapes often increase costs and delay project completion. Additionally, the construction industry's heavy reliance on manual labor poses substantial safety risks for workers, necessitating stringent safety regulations to reduce injury and fatality rates. Furthermore, nearly every stage of traditional construction involves significant energy consumption and results in considerable greenhouse gas emissions [5]. In this context, 3D-concrete printing (3DCP) has emerged as a promising solution to address these challenges. Despite its promising advantages, 3DCP faces significant material challenges, particularly in the design and optimization of printable concrete mixes. Conventional 3D-printed concrete often relies on high binder content to achieve adequate flowability, buildability, and mechanical strength. However, such high cementitious material usage results in increased carbon emissions, contradicting the environmental objectives that 3DCP aims to support. This presents a critical need to explore sustainable alternatives that can maintain or enhance the performance of 3DCP while reducing its environmental impact [6]. Moreover, a printable mix must exhibit sufficient green strength to flow through the distribution system, be deposited in stable layers, and support the weight of subsequent layers without damage. For instance, self-compacting concrete (SCC) with low viscosity is typically desirable for pumping; however, printable mixes require a higher yield stress to ensure layer stability and prevent deformation during the printing process. Supplementary Cementitious Materials (SCMs) such as fly ash (FA), slag, silica fume (SF) and metakaolin (MK) have gained significant attention as viable solutions to these problems. However, the SCMs additions significantly influence the rheological properties of the printable mix. To enhance pumpability by reducing viscosity and to improve buildability by increasing static yield stress after extrusion, thixotropic materials can be incorporated into the cement. These materials reduce viscosity under applied loading shear, facilitating pumping, while increasing yield stress when at rest, thereby improving shape stability and minimizing deformation [7]. Fly Ash (FA) is a fine, powdery material generated as a byproduct during the combustion of coal in coal fired thermal power plants. Widely recognized as a pozzolanic material, FA primarily comprises siliceous and aluminous components. Its particles are typically spherical in shape, with sizes ranging from sub-micron to 300 μm in diameter [8]. Research by Laskar and Talukdar [9] indicates that incorporating small amounts of FA can lower yield stress,

*Corresponding Author.
E-mail address: thajeel.marwah@edu.bme.hu ; Tel: (+36205957378) (Marwah M. Thajeel)

https://doi.org/10.30772/qjes.2025.155882.1448
2411-7773

whereas higher levels of FA replacement may cause a slight increase in yield stress. Similarly, Banfill [10] observes that increasing FA concentration leads to a reduction in both plastic viscosity and yield stress.

Nomenclature

AM	Additive Manufacturing	W_n	Nozzle width
C	Cast specimens	*X*	Load parallel to layer length
H	Layers horizontal	*Y*	Load parallel to layer width
MK	Metakaolin	*Z*	Load parallel to layer height
P	Printed specimens	*SCMs*	Supplementary Cementitious Materials
*P*1	Cubes printed in a zigzag pattern with a 90° rotation in alternate layers	*SF*	Silica Fume
*P*2	Cubes printed in a circular pattern	*SP*	Superplasticizer
*P*3	Cubes printed in a zigzag pattern with exact alignment (odd and even)	*S*1	Shape retention
V	Layers vertical	3*DCP*	3D Concrete Printing
W_f	Average width of the first and last extruded layers	3*DPC*	3D Printed Concrete

Furthermore, Beycioglu and Aruntas [11] highlight that the spherical shape and smooth surface of FA enable self-consolidating concrete mixes to require less water, thereby improving passing ability, flowability, and viscosity. The production of iron and steel in blast furnaces results various types of slag. When blast furnace slag is quickly cooled with water while in its molten form, it changes into glassy, granulated particles [12]. These particles are then ground to form ground granulated blast furnace slag (GGBS), which is classified as a latent hydraulic material due to its pozzolanic and cementitious characteristics [13]. Ahari et al. [14] reported that replacing ordinary Portland cement (OPC) with slag reduced both yield stress and plastic viscosity, regardless of the water-to-binder (w/b) ratio [15, 16]. In contrast, Tattersall [17] observed that incorporating slag into mixes with low cement content (200 kg/m^3) decreased yield stress but increased plastic viscosity. Slag's high specific surface area (SSA) and significant chemical activity necessitate more water compared to cement particles, which can adversely affect the rheological properties of the mixes. Joh et al. [18] found that yield stress decreased with up to 30% slag replacement of OPC but increased beyond 45% replacement, while plastic viscosity consistently decreased with increasing slag content. Riad and Benmalek [16] noted that granular slag and crystalline slag have SSAs of 228 m^2/kg and 485 m^2/kg, respectively, exhibiting cement-like activity. Their study revealed that, compared to cement-based mixes, the plastic viscosity of the granular slag mix dropped from 150 *Pa.s* to121 *Pa.s* due to the absorption of superplasticizer particles, despite granular slag's lower SSA relative to cement. Similarly, the plastic viscosity of the crystalline slag mix decreased from 150 Pa.s to 91 *Pa.s* at the same replacement level. Silica fume (SF) is a by-product formed during the manufacturing of elemental silicon and ferrosilicon alloys. Its particle size typically ranges from 0.1 to 0.3 μm [19]. Panda and Tan [19] observed that incorporating silica fume (SF) improves the yield stress and structural buildability of concrete by improving particle packing density and particle size distribution in fresh concrete. Similarly, Zhang et al. [20] reported that replacing 2% of binder with SF increased the thixotropy and green strength of the mix. For instance, a mix with a water-to-binder ratio of 0.44 containing 12% SF by binder weight exhibited a significant reduction in plastic viscosity. This decrease can be attributed to the lower specific gravity of SF compared to cement, which results in higher binder contents in SF based mixes. Increased packing density fills voids and introduces more lubricant, reducing shear stress and enhancing flowability [21]. Furthermore, the smooth surface and spherical shape of SF particles may contribute to the reduction in plastic viscosity. Interestingly, as the FA replacement ratio increases, the spread diameter also rises, indicating higher slump characteristics in the mixtures. However, adding just 10% SF caused the spread diameter to decrease significantly, from 22.57 *cm* to 10.13 *cm*, highlighting SF's effectiveness in improving yield stress and shape retention capacity [22]. Metakaolin is a highly pozzolanic material with a reactivity comparable to, or even surpassing, that of silica fume [23]. Its particle size can vary depending on the precursor clays used, but is typically smaller than 5 μm [23]. Bohuchval et al. [24] investigated the influence of metakaolin on 3*D* printable concrete mixtures. Their findings indicated that increasing the replacement of clinker with metakaolin enhanced the static yield stress, thereby improving the buildability of the mixtures. However, the high-water demand of metakaolin led to stiff and dry mixes, which adversely affected pumpability and extrudability [24]. Sonebi et al. [25] showed that MK enhances yield stress, which aids in regulating the flow spread of cement paste. The use of MK as a cement substitute in 3D printing is still relatively unexplored. Therefore, additional research is needed to incorporate MK effectively, aiming to enhance the printability and mechanical properties of 3*DCP*. Therefore, this study investigates the integration of metakaolin alongside silica fume into 3*DCP* By systematically analyzing the effects of these SCMs on the fresh and hardened properties of 3D printed concrete, the research aims to provide a pathway for optimizing material formulations in 3*DCP*. The findings are expected to contribute to advancing sustainable practices in the construction industry while addressing the pressing need for high-performance, eco-friendly materials. Moreover, investigates the effect of printing parameters (anisotropy and printing paths) effect on the 3D-printed concrete mechanical properties.

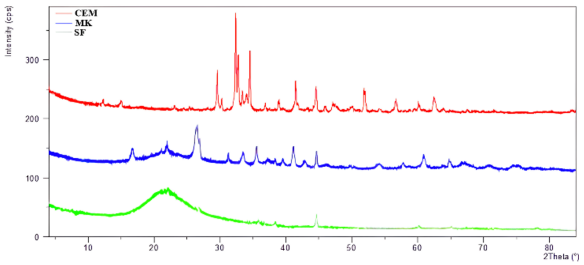

Figure 1. XRD results for the binders.

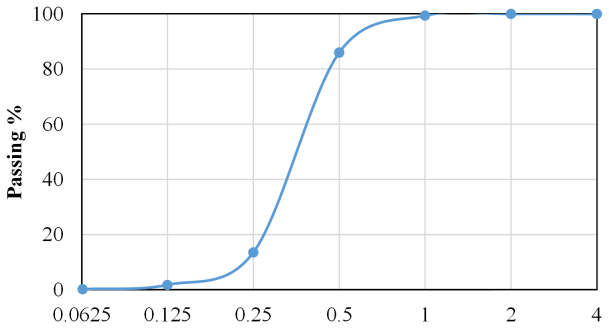

Figure 2. Particle size distribution of the used sand.

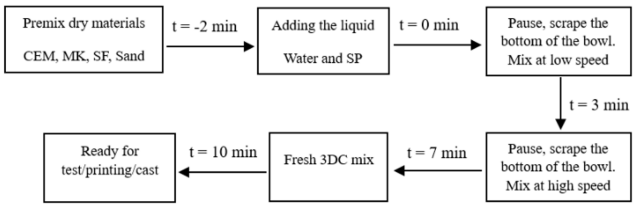

Figure 3. Mixing procedure for the fresh mix preparation.

2. Materials and methods

2.1 Raw materials and mixing procedure

The materials and methods used in this study include Portland cement (*CEM*I52.5*N*) and supplementary cementitious materials (SCMs) such as Metakaolin (MK) and Silica Fume (SF). The chemical compositions and physical properties of these binders were obtained from the manufacturers and are presented in Table 1. X-ray diffraction (XRD) patterns of the raw materials are

shown in Fig. 1. These patterns were recorded using a PANalytical $X'Pert$ Pro MPD diffractometer equipped with an X'Celerator detector. The instrument employed $Cu-K\alpha$ radiation at $40kV$ and $30mA$, with a 2θ scan range from 3°to 85°. The fine aggregate utilized in this research is locally sourced quartz sand with a maximum particle size of 1.2 mm to accommodate the limitations of the pump hose nozzle. The sand had a fineness modulus of 2.99, and its particle size distribution, determined through sieve analysis, is illustrated in Fig. 2. A polycarboxylate ether-based superplasticizer (SP), MasterGlenium 300 (BASF), was chosen to achieve the necessary workability for 3D-printable concrete. Table 2 outlines the specific proportions of the two mixtures investigated. In the first mixture (M-1), 10% of the cement content was replaced with Metakaolin. In the second mixture (M-2), the cement replacement included 10% Metakaolin and an additional 5% Silica Fume to evaluate the influence of Silica Fume on the printability and mechanical characteristics of 3D-printed concrete. All other mixture parameters were kept consistent, including a water-to-binder ratio of 0.33, a sand-to-binder ratio of 1.5, and an SP dosage of 0.45% by binder weight. The mixing process began with a 2-minute dry blending of the binders and sand. Following this, the mixing water and SP were added, and the mixture was stirred at a low speed for 3 minutes to achieve homogeneity. After pausing to scrape the mixing bowl, the mixture was further blended at a higher speed for 3 minutes. Once mixing was completed, the material was immediately tested, printed, or cast into molds. The mixing sequence is depicted in Fig. 3, with the addition of water and SP considered as the starting point ($t = 0\ min$).

Table 1. The chemical compositions and physical characteristics of cementitious materials.

Oxide (wt%)	CEM I 52.5 N	MK	SF
SiO_2	20.59	52-53	96.43
$Al2O_3$	05.55	43-44	00.70
Fe_2O_3	03.21	01.50	00.073
CaO	65.02	00.50	00.78
MgO	01.44	00.40	00.70
SO_3	02.88	-	00.038
$K2O$	00.78	02.00	01.28
Cl	00.0048	-	-
Na_2O	-	00.10	-
TiO_2	-	01.00	-
LOI		01.59	02.80
Density (g/cm^3)	03.17	02.60	02.15
SSA (cm^2/g)	4500	22000	20000

2.2 3D concrete printing (3DCP) setup

In this study, a MUITIMIX-3D mixing pump from MAI Fig. 4a was employed. The machine comprises a multifunctional display, a mixing unit, and a pumping unit. For the purposes of this research, only the pumping unit was employed, while the fresh mixtures were externally prepared with a Hobart mixer and manually loaded into the pump to ensure accurate material ratios and maintain consistent mixing procedures. The pumping system itself, responsible for transferring the mixture to the print head, includes a motor, a hopper equipped with a feed screw, a pump, and a hose connection. The printing process was carried out using a six-axis robotic arm from ABB Fig. 4b. This robotic arm can perform printing tasks with 360-degree rotation, covering a horizontal diameter of up to 3 meters and a vertical height of 3 m, which can extend to 6 m. The printing speed of the robotic arm can vary between 0 mm/s and 200 mm/s. The movement of the robotic arm's head is controlled by a connected controller. A flexible hose with a 25 mm internal diameter and 5 m in length was used to link the pump to the nozzle mounted on the end of the z-axis of the robotic print head. The nozzle used in this study had a 25 mm diameter. For all the mixes, the speed of printing, the rate of flow, and height of the layer were standardized at 84 mm/s, 1.5 L/min, and 10 mm, respectively.

3. Test procedures

3.1 Rheological tests

The evolving rheological characteristics of the printing material play a crucial role in the success of 3D printing. Effective printing requires balancing two competing demands: flowability and buildability of fresh mixture. On one side, the mixture must possess sufficient fluidity to ensure smooth extrusion through the nozzle without blockages. On the other side, it must have adequate stiffness to support its own weight and the increasing vertical load from additional layers without requiring further support after extrusion. Achieving this balance necessitates that the extruded material maintains its shape and remains stable. This demands careful design and fine-tuning of the printing material's properties to facilitate appropriate rheological transitions from mixing through filament deposition to hardening.

Table 2. Mix proportions of the used mixtures.

Type	CEM (wt%)	Bi MK (wt%)	SF (wt%)	Sand (wt%)	Water (wt%)	SP (wt%))
M-1	90	10	00	150	33	0.45
M-2	85	10	05	150	33	0.45

(a)

(b)

Figure 4. 3DCP setup, (a) Mixing pump, (b) Printing robot.

The flowability of printing concrete is a key factor for successful extrusion, as it ensures the ease, consistency, and stability required to produce a well-controlled filament through the nozzle. In this study, the flow table test was used to evaluate the flowability of fresh mixtures, following the guidelines of EN 1015-3 [26]. The test employed a mini-cone mold with internal dimensions of 70 mm at the top, 100 mm at the base, and a height of 60 mm. The interior surface of the mold was lubricated with mold oil before testing. The fresh mixture was added in two stages: the first half of the mold was filled and tamped approximately 10 times using a wooden stick, and the process was repeated for the remaining half. The surplus material was evenly smoothed with a trowel. Following the removing of the mold, the flow table dropped 15 times within a 15-second period. The resulting spread diameter was then measured in two perpendicular directions to document the results, as shown in Fig. 5. For each mixture, this test was performed at intervals of 10 minutes, from 10

minutes to 60 minutes after mixing. To minimize water evaporation, the fresh material was stored in a sealed plastic bag. Each test was repeated three times for accuracy. Shape retention is the ability of an extruded concrete layer to preserve its cross-sectional dimensions, corresponding to the nozzle's shape. To evaluate this property, a hollow rectangular structure measuring 200 *mm* in width and 400 *mm* in length was printed, as shown in Fig. 6a. The width of the printed segments was measured using a vernier caliper to determine the shape retention ratio (S_1). This ratio, introduced by Panda et al. [27], is expressed as, Eq. 1.

$$S1 = W_f / W_n \tag{1}$$

where W_f represents the average width of the first and last extruded layers (measured at each side of the rectangular), and W_n is the nozzle width. An S_1 value closer to 1 indicates superior shape retention. Buildability refers to the capacity of printable material to maintain its form without excessive deformation or structural failure. One of the simplest methods to assess buildability is by determining the maximum height of a printed structure that can be achieved without failure under consistent printing conditions. In this study, as illustrated in Fig. 7a, a 200 *mm* wall was printed to evaluate buildability. The number of filament layers successfully printed was used as a measure of buildability, with any noticeable deformation or collapse of the structure indicating a failure in buildability.

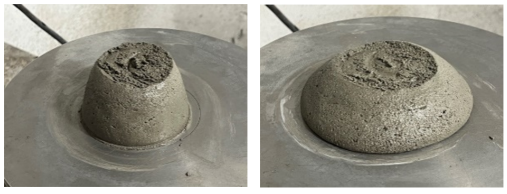

(a) (b)

Figure 5. Flow table test, (a) before and, (b) after dropped the table.

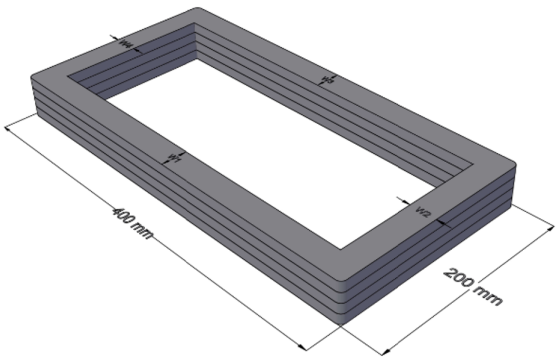

Figure 6. 3DP rectangular for shape retention test.

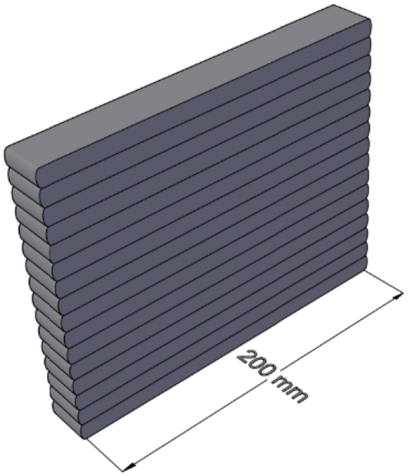

Figure 7. 3DP wall for evaluating buildability.

3.2 Compressive strength test

A wall with dimensions of $750 \times 100 \times 50\ mm^3$ was printed. From this wall, $40 \times 40 \times 40\ mm^3$ cubes were cut. To evaluate the anisotropic mechanical characteristics of the printed mortar, the samples were tested along the X, Y, and Z axes Fig. 8, with four tests performed in each orientation [28, 29]. The results were averaged for each direction. In total, twelve printed cubes were prepared and tested for each mixture. Additionally, four cast cubes of identical dimensions were created and tested for comparison. All specimens were cured at ambient room temperature, and compressive strength was measured at 28 days at a loading rate of 2.4 kN/s in accordance with EN 12390-3 [30].

3.3 3.3. Printing parameters effect

The M-2 mixture was used to check the effect of the printing parameters.

3.3.1 Anisotropy

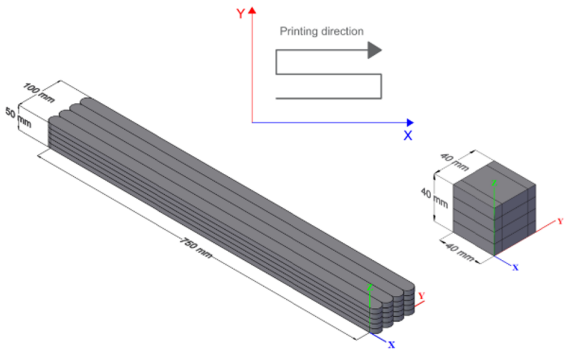

Figure 8. 3DP wall and load directions for compressive strength testing of printed cubes.

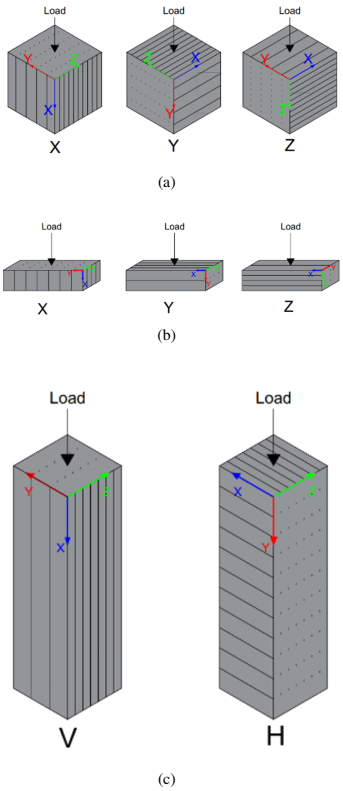

Figure 9. Load directions for assessing anisotropy effects on the mechanical properties of 3DPC.

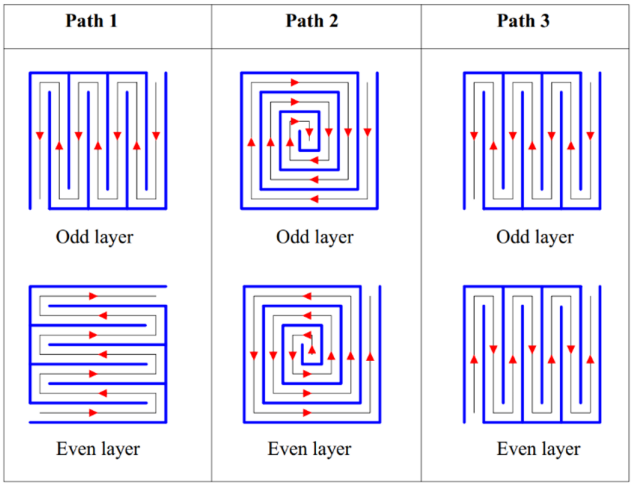

Figure 10. Schematic representation of printing paths.

Figure 11. 3DPC cubes before and after surface smoothing.

This section examines the impact of anisotropy on the mechanical properties of 3D-printed concrete. Cubes measuring $100 \times 100 \times 100\ mm^3$ were extracted from a printed slab with dimensions of $580 \times 286 \times 110 mm^3$ to evaluate compressive strength. Tests were conducted in the X, Y, and Z directions Fig. 9a following EN 12390-3 [30], with a loading rate of 5 kN/s, and three tests were repeated in each direction. To assess the anisotropy effect on flexural strength, prisms measuring $40 \times 40 \times 160 mm^3$ were cut from a printed slab with dimensions of $580 \times 320 \times 90\ mm^3$. These prisms were also tested in the X, Y, and Z directions Fig. 9b. Three tests were performed for each direction, and the average values were calculated. Testing adhered to EN 12390-5 [31], with a loading rate of 0.05 kN/s. Additionally, prisms with dimensions of $70 \times 70 \times 250 mm^3$ were taken from the same slab to evaluate the anisotropy effect on the modulus of elasticity. These specimens were tested in two orientations: horizontal (H) and vertical (V) with respect to the printed layers Fig. 9c. Three repeated tests were conducted in each direction, and the average results were determined according to the EN 12390-13 [31] standard. For all mechanical tests, cast specimens with identical dimensions and quantities to the 3D-printed samples were prepared for comparison. All samples were cured at room temperature until testing at 28 days.

3.3.2 Printing path

To investigate the impact of printing paths on compressive strength, 150 mm cubes were printed using three distinct path patterns, as shown in Fig. 10a. Three identical cubes were printed for each path configuration. Path 1 consisted of a zigzag pattern for the odd layers, with the even layers rotated 90°. Path 2 featured layers printed in a circular pattern, while Path 3 employed zigzag layers aligned in the same orientation for both odd and even layers. Figure 10a provides a schematic representation of these printing paths. After printing, the cubes were stored under laboratory conditions and tested at 28 days of age. Two days prior to testing, the top surfaces of the printed cubes were smoothed to ensure uniform load distribution during testing, as depicted in Fig. 11. For comparison, three cast cubes of the same dimensions were also prepared and tested under identical conditions.

4. Results and discussion

4.1 Rheological properties

4.1.1 Flowability

Figure 12 shows the test data of flowability from 10 min to 60 min after liquid addition. The flowability test results indicate that both mixtures exhibit adequate spread diameters for printability purposes. However, a noticeable difference is observed between the two mixes in terms of fluidity. Mix M-1, which replaces 10% of cement with metakaolin, demonstrates higher fluidity compared to Mix M-2, which incorporates 10% metakaolin and 5% silica fume. While the enhanced fluidity of M-1 may facilitate better extrusion, it compromises shape stability, making it unsuitable for maintaining structural integrity during buildability tests. In contrast, Mix M-2 achieves a balance between flowability and buildability, producing continuous and intact filaments within the designated open time. This suggests that Mix M-2 is more compatible with 3D-printing requirements, particularly for setups utilizing a cavity pump to extrude material directly from the hopper. By retaining shape stability after extrusion, Mix M-2 enables successful layer stacking, which

is essential for additive manufacturing processes. Given the inherent conflict between achieving sufficient flowability and maintaining desired buildability, it is critical to harmonize the rheological properties of the material. Mix M-2 demonstrates an optimal balance, ensuring smooth extrusion while preserving the ability to retain its shape post-extrusion, making it the more suitable choice for this specific printing setup.

4.1.2 Shape retention

The shape retention results, as shown in Fig. 13, indicate a clear distinction between the two mixes. M-1 exhibited an S_1 value of 1.18, which is slightly above the ideal value of 1. This suggests that the extruded filament from M-1 experienced slight over-expansion beyond the nozzle's cross-sectional area. Such over-expansion can indicate excessive fluidity, which compromises the material's ability to retain its shape and makes it less suitable for buildability. On the other hand, M-2 achieved an S_1 value of 0.99, which is nearly perfect and very close to the ideal value of 1. This result highlights the superior shape retention capability of M-2, as it maintains the extruded filament's dimensions with minimal deformation. The inclusion of both metakaolin and silica fume in M-2 appears to improve its rheological properties, striking an optimal balance between flowability and buildability. Overall, the results demonstrate that M-2 is better suited for 3D-concrete printing applications, as it ensures near-perfect shape retention, enabling precise and consistent layer stacking essential for structural integrity.

4.1.3 Buildability

Fig. 14 demonstrates the buildability results of the two mixes. The difference in the number of layers is indicative of the superior structural stability and load-bearing capacity of M-2 during the printing process. M-1 exhibited limited buildability, supporting up to 29 layers due to its relatively lower shape stability. This could be attributed to the absence of additional fine materials that enhance cohesion and reduce deformation under the weight of subsequent layers. In contrast, M-2, which replaced 10% metakaolin and added 5% silica fume, displayed remarkable buildability, supporting up to 29 layers. The addition of silica fume likely played a crucial role, as its ultra-fine particles improve packing density, interlayer adhesion, and cohesiveness of the mixture. This enhanced stability allows for a more robust stacking of layers without visible deformation or collapse. The results indicate a 164% increase in the number of printed layers when silica fume is added to the mix alongside metakaolin. The improved buildability of M-2 can be attributed to the incorporation of silica fume alongside metakaolin. Silica fume is known for its high surface area and pozzolanic properties, which enhance particle packing and cohesion within the mixture. These characteristics contribute to improved shape stability and interlayer adhesion, which are critical for sustaining taller printed structures. In contrast, M-1, which contains only metakaolin as a replacement material, exhibited weaker shape retention and cohesion, limiting its ability to sustain higher layers without deformation.

4.1.4 Compressive strength results

Figure 15 shows the compressive strength results for the M-1 and M-2 mixes. As is clear from the figure, the compressive strength of cast cubes is consistently higher than that of the 3D-printed cubes for both mixes. Attributes the lower strength in 3D-printed cubes to the 3D-printing process, inherently creating layers with interfaces that are not as well-bonded as the monolithic structure achieved in cast cubes.

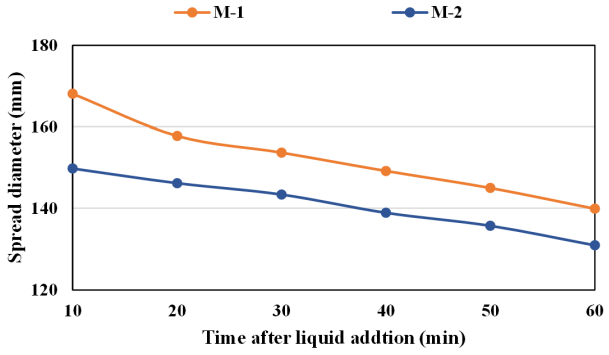

Figure 12**.** Flowability test results.

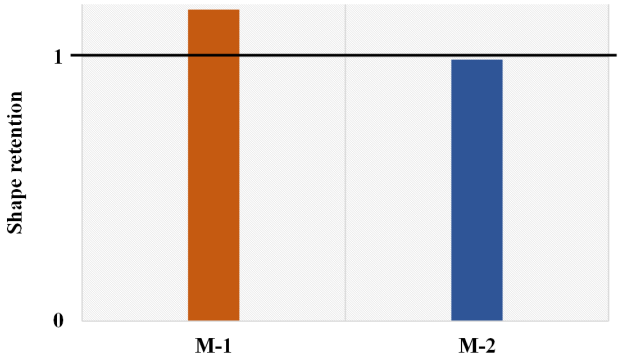

Figure 13**.** Shape retention results.

(a) Model 01 (b) Model 02

Figure 14**.** Buildability results, (a) M-1 (11 layers), (b) M-2 (29 layers).

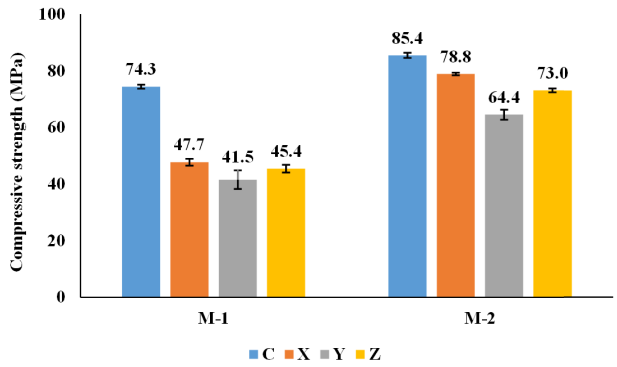

Figure 15**.** Compressive strength results of the two mixes.

Additionally, anisotropy in compressive strength was observed in the printed samples. Anisotropy refers to the variation in strength based on the direction of the applied load relative to the printed layers. This behavior contrasts with cast cubes, which typically exhibit isotropic properties due to their homogeneous structure. In particular, the X direction (aligned with the printing path) exhibited greater compressive strength compared to the Y and Z directions. During printing, the extrusion process aligns particles along the filament direction, leading to better particle packing and material cohesion within the layers in the X direction. M-2 exhibited approximately 15% higher compressive strength in the cast cubes compared to M-1. This improvement is attributed to the addition of silica fume, which enhances particle packing density and overall material strength. In the printed cubes, the compressive strength of M-2 showed even greater increases of approximately 65%, 55%, and 61% in the X, Y, and Z directions, respectively. These substantial improvements underscore the critical role of silica fume in strengthening interlayer bonding and cohesion, particularly along the layer length, resulting in superior performance in 3D-printed samples.

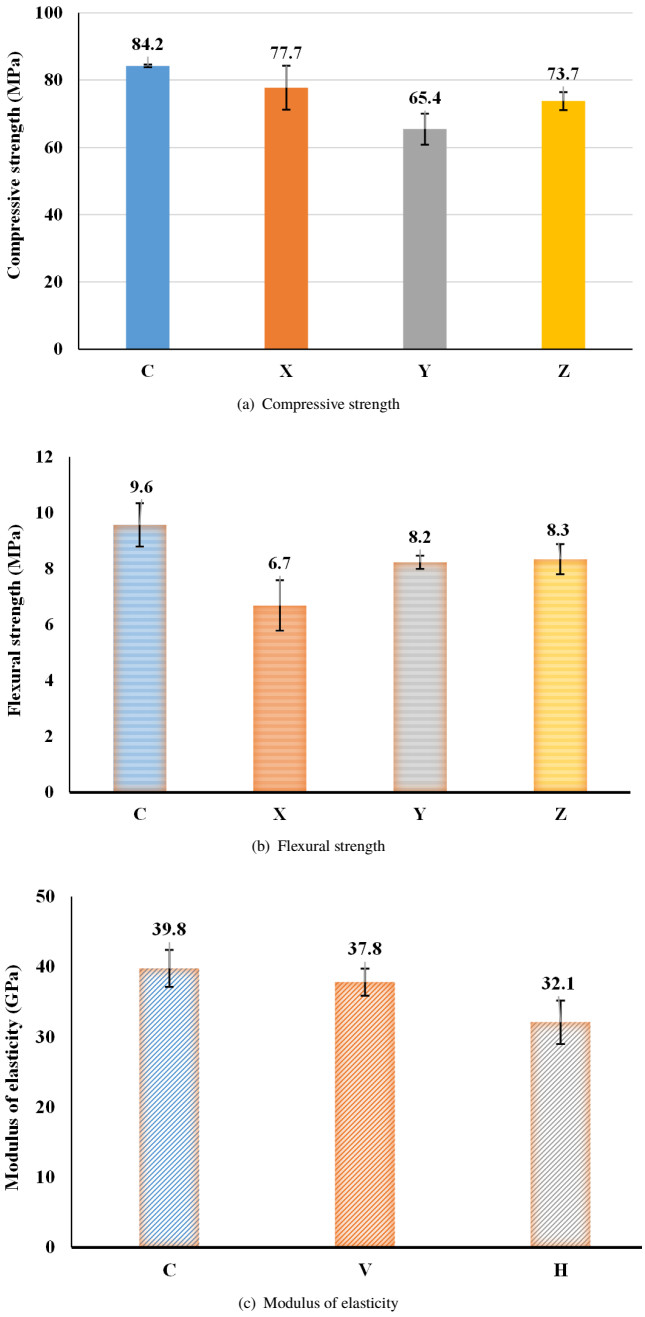

(a) Compressive strength

(b) Flexural strength

(c) Modulus of elasticity

Figure 16**.** Anisotropy results data that show the effect of anisotropy on the mechanical properties of mix M-2.

4.2 Printing parameters results

4.2.1 Anisotropy

The compressive strength results for the cast (C) and 3D-printed cubes reveal significant anisotropy in the mechanical properties of the printed specimens, Fig. 16a. The cast cubes exhibit a uniform compressive strength of 84.15 *MPa*, serving as a baseline for comparison. However, in the 3D-printed cubes, the strength varies depending on the loading direction, with values of 77.67 *MPa* (X), 65.44 *MPa* (Y), and 72.98 *MPa* (Z). This variation highlights the influence of anisotropy in the printed material. Specifically, the X direction (parallel to the layer length) shows the highest compressive strength among the printed cubes, as the load is aligned with the layer length. This strength is attributed to better particle alignment and compaction during the extrusion process along the printing axis. The strength in the X direction is 77.67 *MPa*, which is approximately 92.3% of the cast cube strength (84.15 *MPa*), showing only a slight reduction compared to the cast cubes. Conversely, the *Y* direction (parallel to the layer width) has the lowest compressive strength, likely due to weaker bonding and reduced compaction between filaments in this orientation. The strength in the *Y* direction is 65.44 *MPa*, representing about 77.7% of the cast cube strength, indicating a significant reduction in strength due to the anisotropy of the printed material. The *Z* direction (parallel to the layer height) demonstrates intermediate strength, reflecting the inherent weakness at the interlayer interfaces caused by limited adhesion and potential microvoids during the layer-by-layer deposition process. The strength in the *Z* direction is 72.98 *MPa*, which is approximately 86.8% of the cast cube strength. It also shows a reduction compared to the cast samples, but is higher than the Y direction. The flexural strength results for the cast and 3D-printed prisms provide further insight into the anisotropic behavior of the material, Fig. 16b. The flexural strength of the cast prisms is 9.6 *MPa*, which serves as a reference value. In the 3D printed prisms, the flexural strength varies depending on the direction of loading, with values of 6.7 *MPa* (X), 8.2 *MPa* (Y), and 8.3 *MPa* (Z). The flexural strength in the X direction is 6.7 *MPa*, which represents approximately 69.8% of the flexural strength of the cast prisms (9.6 *MPa*). This reduction in strength is attributed to the weaker interlayer bonding along the printing path, where the filament alignment may not be as cohesive as in other directions. The lower strength in the *X* direction indicates that the material experiences greater deformation before failure compared to the cast prisms. However, the flexural strength in the Y direction increases to 8.2 *MPa*, which is about 85.4% of the cast value. This improvement suggests that the alignment and compaction between layers are better in the width direction compared to the *X* direction. However, the strength is still lower than that of the cast prisms, which can be attributed to the interlayer bonding strength not being as optimal as it would be in a more homogeneous cast material. Meanwhile, the Z direction, where the load is applied perpendicular to the printed layers, shows a flexural strength of 8.3 MPa, which is approximately 86.5% of the cast value. The relatively higher strength in the *Z* direction, compared to the *X* direction, suggests that the interlayer bonding in the vertical direction is better, possibly due to the nature of the printing process and the compaction of the material during deposition. The modulus of elasticity results are presented in Fig. 16c. The modulus of elasticity for the cast prisms is 39.8 *GPa*, serving as a reference value for the material's stiffness. The printed prisms were evaluated in two orientations: V (vertical), where the force is applied along to the printed layers, and H (horizontal), where the force is applied across to the printed layers. In the V orientation, the modulus of elasticity of the printed prisms is 37.8 *GPa*, which is approximately 94.9% of the modulus of elasticity of the cast prisms (39.8 *GPa*). This slight reduction in stiffness suggests that while the material's alignment along the vertical direction (layer orientation) does not cause a significant decrease in stiffness, there is still a slight weakening due to the inherent nature of the 3D-printing process. The material in this direction performs similarly to the cast material, but the interlayer bonding and slight misalignments still reduce the overall stiffness compared to the cast material. When the load is applied in the H direction, perpendicular to the printed layers, the modulus of elasticity of the printed prisms is 32.1 *GPa*, which is approximately 80.7% of the modulus of elasticity of the cast prisms. This substantial decrease in stiffness indicates that the horizontal orientation (across the layers) suffers a greater loss in material stiffness. The reduction in modulus in this direction is likely due to the poor interlayer bonding and the weaker cohesion between the printed layers. The material in this direction is more susceptible to deformation under stress, leading to a noticeable reduction in modulus.

4.2.2 Printing path

Figure 17 shows the printing path effect on the compressive strength. As shown the cast cubes have the highest compressive strength while the printed cubes show a compressive strength with a reduction by about 11.7%, 26.5% and 14.1% in P1, P2, P3 respectively, compared to the cast cubes. In Path 1 (P1), where layers are printed in a zigzag pattern with a 90-degree rotation in alternate layers, showed the highest compressive strength among the printed specimens. The alternating orientation of layers helps to distribute stresses more evenly and reduce the impact of weak interlayer bonds. This printing pattern mimics a more isotropic structure, which improves strength, though it still doesn't match the uniformity of cast specimens. While Path 2 (P2), which uses a circular printing pattern, exhibited the lowest compressive strength. In circular paths, the alignment of the printed filaments can create concentric layers where stress might concentrate, leading to weaker points in the structure. The circular pattern may also cause inconsistencies in the bonding between layers, especially in the center, leading to a significant reduction in compressive strength. Meanwhile, Path 3 (P3), where layers are printed in a zigzag pattern with exact alignment in both odd and even layers, resulted in compressive strength higher than Path 2 but lower than Path 1. The consistent alignment of the layers in the same direction (zigzag) means that any weakness in one layer could propagate through subsequent layers, reducing overall strength. However,

it still performs better than the circular path due to better stress distribution, but not as well as the alternating zigzag pattern of Path 1.

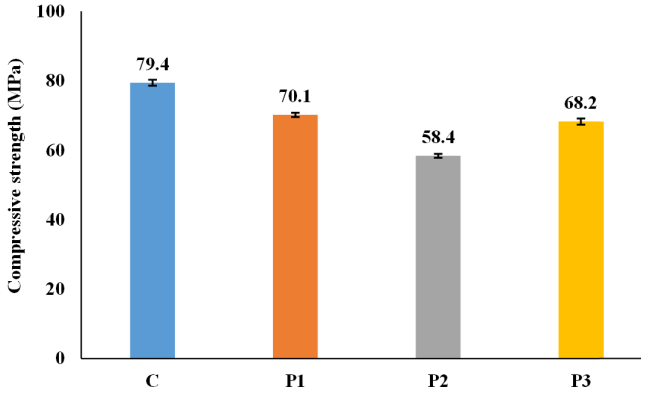

Figure 17**.** Printing path results.

5. Conclusions

Based on the comprehensive study of 3D-printed concrete mixtures and their properties, the following conclusions can be drawn:

1. Rheological properties:
   - Mix M-2 (85% cement, 10% metakaolin, 5% silica fume) demonstrated superior performance compared to M-1 (90% cement, 10% metakaolin) in terms of flowability, shape retention, and buildability.
   - M-2 achieved an optimal balance between flowability and buildability, with a near-perfect shape retention ratio of 0.99.
   - The addition of silica fume in M-2 significantly improved buildability, allowing for 163.64% more printed layers compared to M-1.
2. Compressive strength:
   - 3D printed specimens consistently showed lower compressive strength compared to cast specimens due to layering effects and anisotropy.
   - M-2 exhibited approximately 15% higher compressive strength in cast cubes and 55-65% higher strength in printed cubes compared to M-1, highlighting the beneficial effect of silica fume addition.
3. Anisotropy:
   - Significant anisotropy was observed in the mechanical properties of 3D-printed specimens.
   - Compressive strength was highest in the X direction (parallel to the printing path), followed by the Z direction (layer height), and lowest in Y direction (layer width).
   - Flexural strength showed a different trend, with the Z and Y directions performing better than the X direction.
   - The modulus of elasticity was higher when loaded parallel to the printed layers (V direction) compared to perpendicular loading (H direction).
4. Printing path effect:
   - The zigzag pattern with 90°rotation between layers (P1) showed the highest compressive strength among printed specimens.
   - Circular printing patterns (P2) resulted in the lowest compressive strength.
   - Consistent zigzag patterns (P3) performed better than circular patterns but worse than alternating zigzag patterns.

These findings highlight the importance of mix design, printing parameters, and loading direction considerations in optimizing the performance of 3D-printed concrete structures. The study demonstrates that careful selection of supplementary cementitious materials and printing strategies can significantly enhance the mechanical properties and buildability of 3D-printed concrete.

Authors' contribution

All authors contributed equally to the preparation of this article.

Declaration of competing interest

The authors declare no conflicts of interest.

Funding source

This study is funded by the Stipendium Hungaricum Scholarship Program.

Data availability

The data that support the findings of this study are available from the corresponding author upon reasonable request.

Acknowledgements

The authors would like to acknowledge Dr. Sándor Sólyom and Balázs Burai for their assistance with the printing process and laboratory testing.

REFERENCES

[1] S. Ismail and M. Ramli, "Engineering properties of treated recycled concrete aggregate (rca) for structural applications," *Construction and Building Materials*, vol. 44, pp. 464–476, 2013. [Online]. Available: https://doi.org/10.1016/j.conbuildmat.2013.03.014

[2] B. Nematollahi, M. Xia, and J. Sanjayan, *Current progress of 3D concrete printing technologies*. IAARC Publications, 2017, vol. 34.

[3] S. H. Reddy, K. M. Peera, A. Surendra, C. Arvind kumar, and M. Leelakar, "Role of nano-al2o3 in modifying the properties of ultra high performance concrete," *Al-Qadisiyah Journal for Engineering Sciences*, vol. 18, no. 1, pp. 72–77, 2025. [Online]. Available: https://qjes.qu.edu.iq/article_186243.html

[4] S. H. Ghaffar, J. Corker, and P. Mullett, *The potential for additive manufacturing to transform the construction industry*. Routledge, 2020.

[5] H. Yan, Q. Shen, L. C. Fan, Y. Wang, and L. Zhang, "Greenhouse gas emissions in building construction: A case study of one peking in hong kong," *Building and environment*, vol. 45, no. 4, pp. 949–955, 2010. [Online]. Available: https://doi.org/10.1016/j.buildenv.2009.09.014

[6] S. Paritala, K. K. Singaram, I. Bathina, M. A. Khan, and S. K. R. Jyosyula, "Rheology and pumpability of mix suitable for extrusion-based concrete 3d printing–a review," *Construction and Building Materials*, vol. 402, p. 132962, 2023. [Online]. Available: https://doi.org/10.1016/j.conbuildmat.2023.132962

[7] B. Panda and M. J. Tan, "Experimental study on mix proportion and fresh properties of fly ash based geopolymer for 3d concrete printing," *Ceramics International*, vol. 44, no. 9, pp. 10 258–10 265, 2018. [Online]. Available: https://doi.org/10.1016/j.ceramint.2018.03.031

[8] B. Panda, C. Unluer, and M. J. Tan, "Investigation of the rheology and strength of geopolymer mixtures for extrusion-based 3d printing," *Cement and Concrete Composites*, vol. 94, pp. 307–314, 2018. [Online]. Available: https://doi.org/10.1016/j.cemconcomp.2018.10.002

[9] A. I. Laskar and S. Talukdar, "Rheological behavior of high performance concrete with mineral admixtures and their blending," *Construction and Building materials*, vol. 22, no. 12, pp. 2345–2354, 2008. [Online]. Available: https://doi.org/10.1016/j.conbuildmat.2007.10.004

[10] P. F. G. Banfill, "Rheological methods for assessing the flow properties of mortar and related materials," *Construction and Building materials*, vol. 8, no. 1, pp. 43–50, 1994. [Online]. Available: https://doi.org/10.1016/0950-0618(94)90007-8

[11] A. Beycioğlu and H. Y. Aruntaş, "Workability and mechanical properties of self-compacting concretes containing llfa, gbfs and mc," *Construction and building materials*, vol. 73, pp. 626–635, 2014. [Online]. Available: https://doi.org/10.1016/j.conbuildmat.2014.09.071

[12] G. Ma, Z. Li, and L. Wang, "Printable properties of cementitious material containing copper tailings for extrusion-based 3d printing," *Construction and building materials*, vol. 162, pp. 613–627, 2018. [Online]. Available: https://doi.org/10.1016/j.conbuildmat.2017.12.051

[13] W. Huang, H. Kazemi-Kamyab, W. Sun, and K. Scrivener, "Effect of replacement of silica fume with calcined clay on the hydration and microstructural development of eco-uhpfrc," *Materials & Design*, vol. 121, pp. 36–46, 2017. [Online]. Available: https://doi.org/10.1016/j.matdes.2017.02.052

[14] R. S. Ahari, T. K. Erdem, and K. Ramyar, "Thixotropy and structural breakdown properties of self-consolidating concrete containing various supplementary cementitious materials," *Cement and Concrete Composites*, vol. 59, pp. 26–37, 2015. [Online]. Available: https://doi.org/10.1016/j.cemconcomp.2015.03.009

[15] X. Zhang and J. Han, "The effect of ultra-fine admixture on the rheological property of cement paste," *Cement and concrete research*, vol. 30, no. 5, pp. 827–830, 2000. [Online]. Available: https://doi.org/10.1016/S0008-8846(00)00236-2

[16] R. Derabla and M. L. Benmalek, "Characterization of heat-treated self-compacting concrete containing mineral admixtures at early age and in the long term," *Construction and Building Materials*, vol. 66, pp. 787–794, 2014. [Online]. Available: https://doi.org/10.1016/j.conbuildmat.2014.06.029

[17] G. H. Tattersall, *Workability and quality control of concrete*. CRC Press, 1991.

[18] C. Joh, J. Lee, T. Q. Bui, J. Park, and I.-H. Yang, "Buildability and mechanical properties of 3d printed concrete," *Materials*, vol. 13, no. 21, p. 4919, 2020. [Online]. Available: https://doi.org/10.3390/ma13214919

[19] D. Dey, D. Srinivas, B. Panda, P. Suraneni, and T. Sitharam, "Use of industrial waste materials for 3d printing of sustainable concrete: A review," *Journal of cleaner production*, vol. 340, p. 130749, 2022. [Online]. Available: https://doi.org/10.1016/j.jclepro.2022.130749

[20] Y. Zhang, Y. Zhang, G. Liu, Y. Yang, M. Wu, and B. Pang, "Fresh properties of a novel 3d printing concrete ink," *Construction and building materials*, vol. 174, pp. 263–271, 2018. [Online]. Available: https://doi.org/10.1016/j.conbuildmat.2018.04.115

[21] V. Malhotra, "The rheology of fresh concrete," *Canadian Journal of Civil Engineering*, vol. 11, pp. 135–135, 1984. [Online]. Available: https://doi.org/10.1139/l84-022

[22] P. Mehta and O. Gjørv, "Properties of portland cement concrete containing fly ash and condensed silica-fume," *Cement and Concrete research*, vol. 12, no. 5, pp. 587–595, 1982. [Online]. Available: https://doi.org/10.1016/0008-8846(82)90019-9

[23] C. Li, H. Sun, and L. Li, "A review: The comparison between alkali-activated slag (si+ ca) and metakaolin (si+ al) cements," *Cement and concrete research*, vol. 40, no. 9, pp. 1341–1349, 2010. [Online]. Available: https://doi.org/10.1016/j.cemconres.2010.03.020

[24] M. Bohuchval, M. Sonebi, S. Amziane, and A. Perrot, "Effect of metakaolin and natural fibres on three-dimensional printing mortar," *Proceedings of the Institution of Civil Engineers-Construction Materials*, vol. 174, no. 3, pp. 115–128, 2021. [Online]. Available: https://doi.org/10.1680/jcoma.20.00009

[25] M. Sonebi, M. Lachemi, and K. Hossain, "Optimisation of rheological parameters and mechanical properties of superplasticised cement grouts containing metakaolin and viscosity modifying admixture," *Construction and Building Materials*, vol. 38, pp. 126–138, 2013. [Online]. Available: https://doi.org/10.1016/j.conbuildmat.2012.07.102

[26] 2000, n 1015-3. Methods of test for mortar for masonry. Part 3: Determination of consistency of fresh mortar (by flow table).

[27] B. Panda, C. Unluer, and M. J. Tan, "Extrusion and rheology characterization of geopolymer nanocomposites used in 3d printing," *Composites Part B: Engineering*, vol. 176, p. 107290, 2019. [Online]. Available: https://doi.org/10.1016/j.compositesb.2019.107290

[28] K. R. Messer, A. Fahem, A. T. Guthai, and R. P. Singh, "The experimental methods and elastic properties of shale bedding planes materials state-of-the-art review," *Al-Qadisiyah Journal for Engineering Sciences*, vol. 15, no. 2, pp. 126–130, 2022. [Online]. Available: https://qjes.qu.edu.iq/article_179071.html

[29] M. Abdulrehman, A. Moften, A. Noori, M. Mutair, and A. Alkamal, "Investigating the mechanical and physical properties of lightweight geopolymer concrete," *Al-Qadisiyah Journal for Engineering Sciences*, vol. 17, no. 2, pp. 88–96, 2024. [Online]. Available: https://qjes.qu.edu.iq/article_183784.html

[30] EN 12390-3. Testing hardened concrete. Part 3: Compressive strength of test specimens. 2009.

[31] EN 12390-5. Testing hardened concrete. Part 5: Flexural strength of test specimens,2009.

How to cite this article:
Marwah M. Thajeel, Ameen H. Chalawi, and Gy¨orgy L. Bal´azs (2025). 'Printability and strength of 3D-printed concrete: Role of mix design and printing parameters', Al-Qadisiyah Journal for Engineering Sciences, 18(3), pp. 336-344. https://doi.org/10.30772/qjes.2025.155882.1448